

Reflectance-based projection-resolved optical coherence tomography angiography [Invited]

JIE WANG, MIAO ZHANG, THOMAS S. HWANG, STEVEN T. BAILEY, DAVID HUANG, DAVID J. WILSON, AND YALI JIA*

Casey Eye Institute, Oregon Health & Science University, Portland, OR, 97239, USA

*jiaya@ohsu.edu

Abstract: Optical coherence tomography angiography (OCTA) is limited by projection artifacts from the superficial blood vessels onto deeper layers. We have recently described projection-resolved (PR) OCTA that solves the ambiguity between *in situ* flow and flow projection along each axial scan and suppresses the artifact on both *en face* and cross-sectional angiograms. While this method significantly improved the depth resolution of OCTA, the vascular integrity of the deeper layers was not fully preserved. In this study, we propose a novel reflectance-based projection-resolved (rbPR) OCTA algorithm which uses OCT reflectance to enhance the flow signal and suppress the projection artifacts in 3-dimensional OCTA. We demonstrated quantitatively that rbPR improved the vascular connectivity and improved the discrimination of the deeper plexus angiograms in healthy eyes, compared to prior PR-OCTA method. We also demonstrated qualitatively that rbPR removes flow projection artifacts more completely from the outer retinal slab in the eyes with age-related macular degeneration, and preserves vascular integrity of the intermediate and deep capillary plexuses in the eyes with diabetic retinopathy. Additionally, this method improves the resolution of the choriocapillaris and demonstrates details comparable to scanning electron microscopy.

©2017 Optical Society of America

OCIS codes: (110.4500) Optical coherence tomography; (100.0100) Image processing; (100.2960) Image analysis; (170.4470) Ophthalmology.

References and links

1. Y. Jia, S. T. Bailey, T. S. Hwang, S. M. McClintic, S. S. Gao, M. E. Pennesi, C. J. Flaxel, A. K. Lauer, D. J. Wilson, J. Hornegger, J. G. Fujimoto, and D. Huang, "Quantitative optical coherence tomography angiography of vascular abnormalities in the living human eye," *Proc. Natl. Acad. Sci. U.S.A.* **112**(18), E2395–E2402 (2015).
2. S. S. Gao, Y. Jia, M. Zhang, J. P. Su, G. Liu, T. S. Hwang, S. T. Bailey, and D. Huang, "Optical Coherence Tomography Angiography," *Invest. Ophthalmol. Vis. Sci.* **57**(9), OCT27–OCT36 (2016).
3. D. Huang, Y. Jia, and S. S. Gao, "Principles of optical coherence tomography angiography," in *Clinical OCT Angiography Atlas*(2015), p. 3.
4. R. F. Spaide, J. G. Fujimoto, and N. K. Waheed, "Image artifacts in optical coherence tomography angiography," *Retina* **35**(11), 2163–2180 (2015).
5. L. Liu, S. S. Gao, S. T. Bailey, D. Huang, D. Li, and Y. Jia, "Automated choroidal neovascularization detection algorithm for optical coherence tomography angiography," *Biomed. Opt. Express* **6**(9), 3564–3576 (2015).
6. Y. Jia, S. T. Bailey, D. J. Wilson, O. Tan, M. L. Klein, C. J. Flaxel, B. Potsaid, J. J. Liu, C. D. Lu, M. F. Kraus, J. G. Fujimoto, and D. Huang, "Quantitative Optical Coherence Tomography Angiography of Choroidal Neovascularization in Age-Related Macular Degeneration," *Ophthalmology* **121**(7), 1435–1444 (2014).
7. A. Zhang, Q. Zhang, and R. K. Wang, "Minimizing projection artifacts for accurate presentation of choroidal neovascularization in OCT micro-angiography," *Biomed. Opt. Express* **6**(10), 4130–4143 (2015).
8. M. Zhang, T. S. Hwang, J. P. Campbell, S. T. Bailey, D. J. Wilson, D. Huang, and Y. Jia, "Projection-resolved optical coherence tomographic angiography," *Biomed. Opt. Express* **7**(3), 816–828 (2016).
9. G. Chan, C. Balaratnasingam, P. K. Yu, W. H. Morgan, I. L. McAllister, S. J. Cringle, and D.-Y. Yu, "Quantitative Morphometry of Perifoveal Capillary Networks in the Human Retina," *Invest. Ophthalmol. Vis. Sci.* **53**(9), 5502–5514 (2012).
10. K. Singh and R. Kapoor, "Image enhancement using exposure based sub image histogram equalization," *Pattern Recognit. Lett.* **36**, 10–14 (2014).
11. M. Zhang, J. Wang, A. D. Pechauer, T. S. Hwang, S. S. Gao, L. Liu, L. Liu, S. T. Bailey, D. J. Wilson, D. Huang, and Y. Jia, "Advanced image processing for optical coherence tomographic angiography of macular diseases," *Biomed. Opt. Express* **6**(12), 4661–4675 (2015).

12. L. Lam, S.-W. Lee, and C. Y. Suen, "Thinning methodologies-a comprehensive survey," *IEEE Trans. Pattern Anal. Mach. Intell.* **14**(9), 869–885 (1992).
13. D. Huang, Y. Jia, M. Rispoli, O. Tan, and B. Lumbroso, "Optical coherence tomography angiography of time course of choroidal neovascularization in response to anti-angiogenic treatment," *Retina* **35**(11), 2260–2264 (2015).
14. S. S. Gao, L. Liu, S. T. Bailey, C. J. Flaxel, D. Huang, D. Li, and Y. Jia, "Quantification of choroidal neovascularization vessel length using optical coherence tomography angiography," *J. Biomed. Opt.* **21**(7), 076010 (2016).
15. S. M. McClintic, Y. Jia, D. Huang, and S. T. Bailey, "Optical coherence tomographic angiography of choroidal neovascularization associated with central serous chorioretinopathy," *JAMA Ophthalmol.* **133**(10), 1212–1214 (2015).
16. T. S. Hwang, M. Zhang, K. Bhavsar, X. Zhang, J. P. Campbell, P. Lin, S. T. Bailey, C. J. Flaxel, A. Lauer, D. J. Wilson, D. Huang, and Y. Jia, "Projection-resolved optical coherence tomography angiography visualizes capillary nonperfusion in three distinct retinal plexuses in diabetic retinopathy," *JAMA Ophthalmol.* **134**(12), 1411–1419 (2016).
17. M. Zhang, T. S. Hwang, C. Dongye, D. J. Wilson, D. Huang, and Y. Jia, "Automated Quantification of Nonperfusion in Three Retinal Plexuses Using Projection-Resolved Optical Coherence Tomography Angiography in Diabetic Retinopathy," *Invest. Ophthalmol. Vis. Sci.* **57**(13), 5101–5106 (2016).
18. I. Bhutto and G. Lutty, "Understanding age-related macular degeneration (AMD): relationships between the photoreceptor/retinal pigment epithelium/Bruch's membrane/choriocapillaris complex," *Mol. Aspects Med.* **33**(4), 295–317 (2012).
19. G. A. Lutty, "Effects of Diabetes on the EyeEffects of Diabetes on the Eye," *Invest. Ophthalmol. Vis. Sci.* **54**(14), ORSF81–ORSF87 (2013).
20. J. M. Olver, "Functional anatomy of the choroidal circulation: methyl methacrylate casting of human choroid," *Eye (Lond.)* **4**(2), 262–272 (1990).

1. Introduction

Optical coherence tomography angiography (OCTA) is a non-invasive 3-dimensional (3D) tool for imaging retinal and choroidal microvascular networks *in vivo* [1]. It detects flow by evaluating the change in reflectance from sequentially acquired structural OCT images. The 3D nature of the technique allows separate visualization specified vascular layers [2]. However, its depth resolution is limited by the shadowgraphic flow projection artifact, which comes from the time-varying shadows cast by the more superficial blood vessels [3]. On cross-sectional angiograms, this artifact appears as the flow tails below *in situ* blood vessels; on *en face* angiograms, the more superficial plexuses are projected on deeper plexuses. This inability to distinguish between projection artifact and *in situ* flow has confounded the 3D interpretation of OCTA [4].

Initial efforts to suppress projection artifacts from OCTA have relied on the subtraction of superficial signal from deeper slabs [5, 6]. Some have enhanced this technique by factoring in the structural OCT information [7]. These slab subtraction (SS) algorithms require correct segmentation of the vascular layers, which can be problematic in diseased eyes with distorted anatomy. SS also frequently replaces projection artifact with artificial shadows, interrupting the vascular integrity of the deeper layers. Additionally, SS algorithms remove the artifacts only in *en face* angiograms, making cross-sectional angiograms difficult to interpret due to projection artifacts.

Recently, our group proposed a projection-resolved (PR) OCTA algorithm [8] that resolves the ambiguity between *in situ* flow and projection artifact at the level of single voxels, rather than conventional projection removal by SS. Our method is based on the observation that normalized projection artifact signal is less than the value of the original signal. Hence, at each A-scan, signal peaks are successively analyzed, selectively removing those with lesser values than more superficial peaks. The resulting 3D macular angiogram demonstrates 3 distinct retinal vascular plexuses in their true anatomic location, consistent with known histopathology [9]. Even with this method, the continuity of the deeper vasculature is not fully preserved. This is due to an algorithm that relies on A-scans only and assigns decorrelation values of the successive peak positions in a binary fashion.

Here we propose a reflectance-based projection-resolved (rbPR) OCTA algorithm, which improves projection resolution outcomes by using the structural OCT reflectance signal. Details of the image processing steps are described and its performance is evaluated.

2. Data acquisition

OCTA data was acquired using 70 kHz spectral domain OCT system (RTVue-XR Avanti; Optovue, Inc., Fremont, CA) with a center wavelength of 840 nm. Two repeated B-scans, each consisting of 304 A-scans, were captured at each of 304 locations in 2.9 seconds. The 2×2 , 3×3 or 6×6 mm scanning sizes were acquired on the macular regions. A commercial version of the split-spectrum amplitude-decorrelation angiography (SSADA) algorithm detected blood flow. One x-fast and one y-fast scans were acquired, registered, and merged, minimizing motion artifacts.

3. Reflectance-based projection-resolved algorithm

3.1 Overview

A comparison of the C-scan (single voxel thick) of structural OCT (Fig. 1(B)) and OCTA (Fig. 1(F)) at the level of the deep plexus demonstrates that a relationship exists between the vessels, the shadow artifacts, and the projection artifacts. Due to the light attenuation, the superficial blood vessels (Fig. 1(E)) cast shadows in the structural OCT, creating regions with lower reflectance (shadow cast) compared to the surrounding tissue (Fig. 1(C1) and 1(C2)). These areas, however, look brighter in OCTA (Fig. 1(G1) and 1(G2)) due to projection artifacts. This relationship is more obvious in the avascular outer retinal slab (Fig. 1(D) and 1(H)). Furthermore, the capillary patterns on OCTA (Fig. 1(G2)) correspond to the brighter reflectance signal on structural OCT (Fig. 1(C2)). In other words, real vessels correspond to high reflectance while projection artifacts have low reflectance in structural OCT. Therefore, it would be reasonable to utilize the OCT reflectance information obtained from the same C-scan to enhance the contrast of real blood vessels and minimize the projection artifacts. Please note the C-scan mentioned below is single voxel thick.

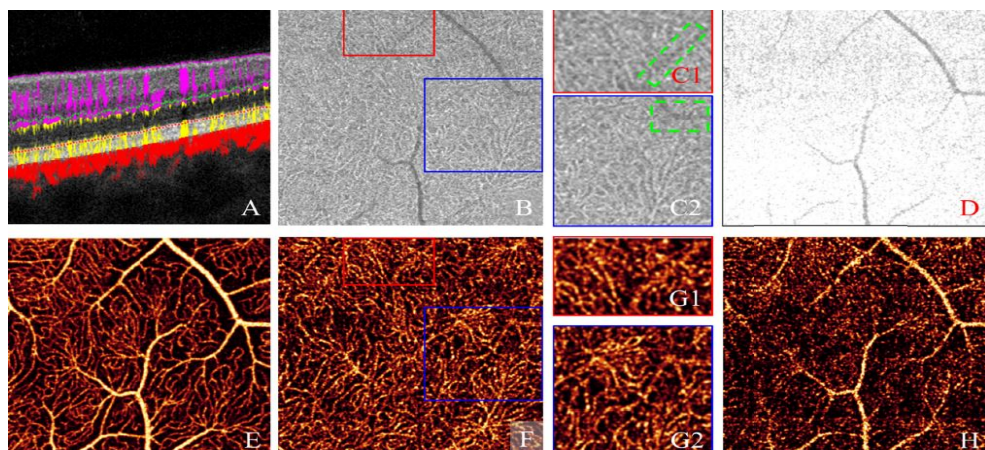


Fig. 1. Illustration of the *in situ* blood flow and flow projection artifact on OCTA and their corresponding signal on structural OCT. (A) Cross-sectional structural OCT (gray) overlaid with OCTA (red). (B) The C-scan of OCT reflectance in deep plexus slab, indicated by yellow dotted line in A. (C1) and (C2) are magnified regions on B to show the vessel shadow artifacts with low reflectance (outlined by green) and the capillary network with high reflectance. (D) The C-scan of OCT reflectance in outer retinal slab, indicated by green dotted line in A. (E) The maximum projection of OCTA in superficial plexus slab, horizontal white dashed line indicates the location of panel A. (F) The C-scan of OCTA in deep plexus slab. (G1) and (G2) are magnified regions on F to show the real capillaries interfered by projection artifact (outline by green). (H) The C-scan of OCTA in outer retinal slab.

Figure 2 summarizes the image processing steps to realize this aim in clinical cases with varied anatomy. First, the structural OCT was divided into two sub-volumes along photoreceptor inner/outer segment (IS/OS). Next, K-means clustering method was applied to obtain vessel contrast enhanced OCT reflectance at each C-scan. A fuzzy C-means method was used to obtain vessel probability distribution map at each C-scan. Then, each angiographic C-scan was scaled by (1) normalized reflectance-based vessel contrast map to suppress projection artifacts, and (2) vessel probability distribution map to enhance the vasculature. This algorithm was implemented with custom software written in Matlab 2016b (*Mathworks, Natick, MA*) installed in a computer with *Intel(R) Core(TM) CPU i7-6800K @3.4GHZ and DDR4 32GB RAM*.

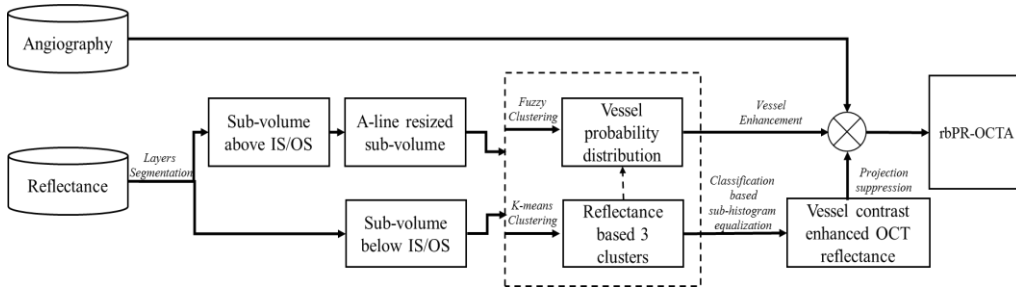


Fig. 2. Overview of the reflectance-based projection-resolved (rbPR) OCTA algorithm. IS/OS: junction of inner and outer photoreceptor.

3.2 Preprocessing

The reflectance of capillaries in inner retina is higher compared to that of the surrounding tissues, while the reflectance of choroidal vascularization (CNV) and normal choroidal vessels is lower compared to that of surrounding tissues, e.g. retinal pigment epithelium (RPE). In the other word, capillaries show different reflectance characteristics in inner and outer retina. To take advantage of the reflectance distribution of blood vessels and better identify them from surrounding tissues, we segmented the scan volume into two sub-volumes: above and below IS/OS volumes [5], and processed them separately. To obtain a homogeneous reflectance C-scan, all A-scans of upper sub-volume (R_a) were resized to a same length D_{max} , which is the maximum distance between ILM and IS/OS layers (Fig. 3(B)). Lower sub-volume (R_b) has a naturally even depth and did not require an adjustment.

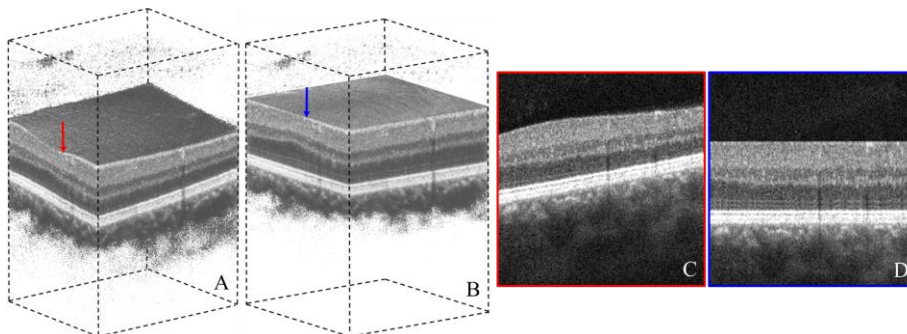


Fig. 3. Illustration of A-line resize. (A) the original reflectance volume; (B) the volume showing resized A-scans above IS/OS . (C) the B-scan of panel A indicated with red arrow. (D) the B-scan of panel B indicated with blue arrow, which shows resized A-scan above IS/OS.

3.3 OCTA projection removal using vessel contrast enhanced OCT reflectance

The reflectance histograms of the volume with 2×2 mm scanning pattern (Fig. 4) illustrate the reflectance distribution. For the whole retinal volume spanning 0.16 mm internal to the ILM and 0.25 mm external to BM (Fig. 4(A)), two inflection points (B_1 and B_2) indicated by red arrows divided the histogram into three parts: high, medium and low reflectance. The voxels of the vitreous, outer nuclear layer (ONL) and shadow artifacts have low reflectance. The reflectance of capillaries and neurosensory retina is between that of the vitreous and the RPE, the nerve fiber layer (NFL) and the large vessels. The histogram of two sub-volumes divided along the IS/OS band (Fig. 4(B) and 4(C)) confirm that capillaries have medium reflectance. Based on this insight, all voxels of each sub-volume were classified into 3 clusters by reflectance and the vascular component can be enhanced in the later steps.

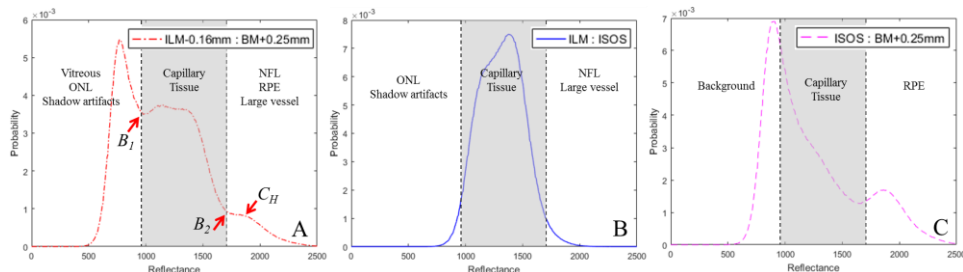


Fig. 4. Illustration of reflectance distribution in whole scan volume (A), volume above photoreceptor inner/outer segment (IS/OS) (B) and volume below IS/OS (C). B_1 and B_2 are boundaries between low, medium and high reflectance. C_H is the center of high reflectance cluster.

In this section, K-means classification was first applied on each sub-volume, and the classification results were used to divide the histogram into sub-histograms in each C-scan. Then the exposure based sub histogram equalization (ESIHE) algorithm [10] was adapted to enhance the blood vessels in each C-scan.

K-means classification method was used to classify the volume into three clusters by minimizing the cost function:

$$LSE_I = \sum_{k=1}^K \sum_{L(i)=k} \|I(i) - C_k\|^2 \quad (1)$$

where, $I(i)$ is the reflectance value of the i -th pixel. k is the cluster index, C_k is the mean reflectance value of the k -th cluster and label $L(i)$ indicates which cluster the i -th voxel belongs to. K is the number of clusters, which is 3 in this application. The classification result was optimized during the iteration of the

$$\left\{ \begin{array}{l} L(i) = k, \arg \min_k \|I(i) - C(k)\|^2 \\ C(k) = \frac{\sum_{L(i)=k} I(i)}{\sum_{L(i)=k} 1} \end{array} \right. \quad (2)$$

The histogram of C-scan was divided into three parts based on the boundaries of the clusters. The divided sub-histograms were equalized to enhance the contrast:

$$I_e(i) = \begin{cases} B_1 \times \sum_{n=0}^{I(i)} \frac{H_c(n)}{N_L} & , 0 \leq I(i) \leq B_1 \\ (B_1 + 1) + (B_2 - B_1 + 1) \sum_{n=B_1+1}^{I(i)} \frac{H_c(n)}{N_M} & , B_1 + 1 \leq I(i) \leq B_2 \\ (B_2 + 1) + (L - B_2 + 1) \sum_{n=B_2+1}^{I(i)} \frac{H_c(n)}{N_H} & , B_2 + 1 \leq I(i) \end{cases} \quad (3)$$

B_1 and B_2 are the reflectance of boundary points among clusters of low, medium and high reflectance. $H_c(n)$ is the original histogram, N_L , N_M and N_H are the numbers of pixels belonging to cluster of low, medium and high. n is the gray value of the reflectance, L is the gray level. I_e is the contrast enhanced image. The resulting enhanced C-scan (Fig. 5(B)) shows the capillaries as brighter and projection artifacts as darker compared to the original C-scan.

Repeating this process on all C-scans of the original reflectance volume (V_o), the vessel contrast enhanced reflectance volume (V_e) could be obtained. Then V_e is used to suppress the projection artifacts (highlighted by arrows in Fig. 5(C) and 5(D)) from superficial vessels (Fig. 1(E)) and to enhance the capillaries in the OCTA C-scans:

$$A_t = A_o \times \text{normalized}(V_e) \quad (4)$$

A_t is the enhanced OCTA volume, A_o represent the original OCTA volume.

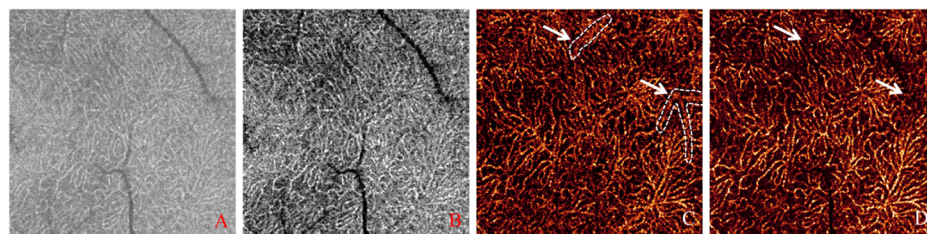


Fig. 5. Illustration of OCTA normalization using vessel contrast enhanced OCT reflectance at deep capillary plexus. (A) the C-scan of original OCT reflectance. (B) the vascular contrast enhanced C-scan. (C) the C-scan of original PR-OCTA. (D) the C-scan processed by normalizing C with B. As highlighted with white outlines, the projection artifacts were removed.

3.4 Capillary enhancement using vessel probability map

Vessel probability maps generated from each reflectance sub-volume individually can be utilized to further improve the normalized OCTA. Specifically, each pixel with a reflectance value between B_1 (boundary value, left red arrow in Fig. 4) and C_H (center value of high reflectance, right red arrow in Fig. 4) is classified into two clusters with a probability using fuzzy C-means method, yielding a probability map P , where P is the probability of pixels belonging to the cluster with higher reflectance. The pixels with a reflectance value out of the range $[B_1, C_H]$ was assigned a probability of 0. In the vessel probability map (Fig. 6(B)), the pixels with higher probability correspond to capillaries. Then this map can be used to further enhance the contrast of the angiogram (Fig. 6(C)):

$$A_r = P \times \text{Normalized}(A_t) \quad (5)$$

The background is darker on the representative C-scan (Fig. 6(C)) and the contrast between vessels and background is improved compared to the unenhanced angiogram (Fig. 6(A)).

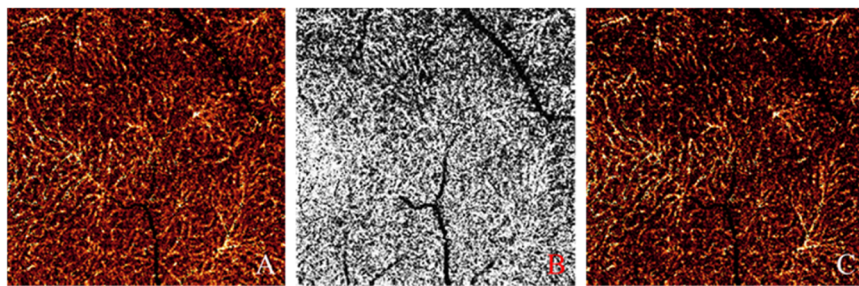


Fig. 6. Vessel probability based vessel enhancement. (A) Projection suppressed C-scan OCTA processed by method described in section 3.3. (B) Vessel probability map calculated by the reflectance. (C) Vessel enhanced vascular image by multiplying A with B.

3.5 Large vessel optimization

The resulting angiogram from the image processing thus far shows a negative artifact at the larger vessels (Fig. 7(B)), because the reflectance of large vessel is larger than C_H , and the reflectance of the region with several voxels thick just below the large vessels is between B_1 and C_H . Therefore, A-scans of the sub-volume containing large vessels were processed separately to remove the negative artifacts at these vessels.

First, large vessels were identified on *en face* inner retinal OCTA by thresholding the upper 5 percentile flow signal. Then, the reflectance of A-scans in the voxels with large vessels were classified into two clusters (low and high reflectance) at boundary B using fuzzy C-means method with a probability. The vessel probability was assigned to 0 if the reflectance is lower than C_h , the mean value of the cluster with high reflectance. The flow signal of the A-scans with large vessels multiplied by the vessel probability produces an angiogram with the large vessels at the correct anatomic location without the negative artifact (Fig. 7(C)).

Figure 8 shows the final results of rbPR-OCTA of the example used in explaining the algorithm.

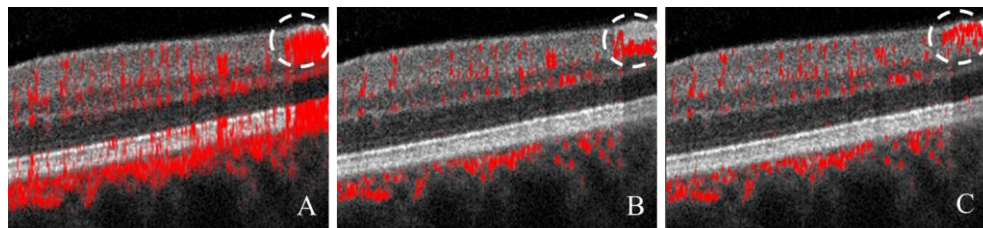


Fig. 7. B-scan reflectance image overlaid with flow signal showing large vessel optimization in rbPR algorithm. (A) Original B-scan. (B) B-scan processed by rbPR without large vessel optimization. (C) B-scan processed by rbPR with large vessel optimization.

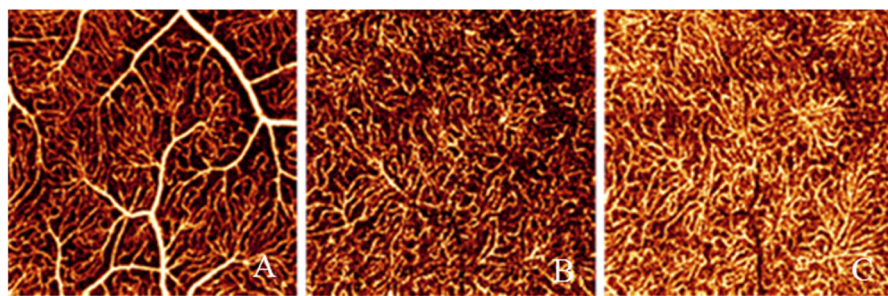


Fig. 8. *En face* maximum projection of rbPR-OCTA in superficial vascular plexus (A), intermediate capillary plexus (B) and deep capillary plexus (C).

4. Comparison and evaluation

Using the acquisition method outlined in previous section, 15 healthy participants, one participant with neovascular age-related macular degeneration and one participant with proliferative diabetic retinopathy were imaged. The diagnosis of the diseased eyes was based on clinical examination, and fluorescein angiography. The participants were enrolled after an informed consent in accordance with an Institutional Review Board approved protocol at Oregon Health and Science University. The study was conducted in compliance with the Declaration of Helsinki.

We processed the images using the PR-OCTA and by the new rbPR-OCTA. Angiograms were segmented into four slabs: superficial, intermediate, and deep retinal plexuses, and the outer retinal slab using structural OCT boundaries [11]. The superficial layer was defined as inner 80% of ganglion cell complex (GCC) which includes all structures between the internal limiting membrane and inner plexiform layer (IPL)/inner nuclear layer (INL) border. The intermediate layer was defined as the outer 20% of GCC and the inner 50% of INL. The deep plexus was defined as the remaining slab internal to the outer boundaries of the outer plexiform layer (OPL). The outer retinal slab was defined as including outer nuclear layer (ONL), photoreceptor layer, the retinal pigment epithelium (RPE), and ending at the Bruch's membrane (BM). *En face* angiograms of each slab were normalized to the same range for the comparison between methods.

4.1 Vascular area, connectivity and contrast

In conventional clinical OCTA, the vascular pattern in the overlaying layers is duplicated in all deeper slabs (Fig. 9(C1)). Using PR methods, we are able to visualize 3 distinct vascular plexuses. Compared to prior PR method, rbPR vascular patterns in intermediate (Fig. 9(B3)) and deep (Fig. 9(C3)) plexuses are better preserved while persistent projection artifacts are suppressed (Fig. 9(D3)). To evaluate this quantitatively, we assessed the vascular skeleton area, vascular connectivity and flow single-to-noise ratio (fSNR) in 15 normal eyes from 15 study participants.

First, we converted the superficial, intermediate and deep plexus angiograms obtained by two different PR methods to binary images based on the thresholds determined from the mean plus 3 standard deviations of the values within their foveal avascular zone (FAZ). Then vascular skeletons (1-pixel wide lines) were detected using thinning methodology algorithm [12]. Vascular skeleton area is defined as the total area of the skeleton network on *en face* angiograms. This parameter was used to evaluate the capability of methods to preserve the number of flow signal. Vascular connectivity is defined as the ratio of the number of connected skeleton pixels to the total number of skeleton pixels. In this step, the connected pixels are detected if the number of the pixel group is larger than five. This measurement was used to assess the capability of methods to preserve the connectivity of vasculatures.

fSNR was calculated from the angiograms as

$$fSNR = \frac{M_{\text{parafovea}} - M_{\text{FAZ}}}{\sigma_{\text{FAZ}}} \quad (6)$$

where, $M_{\text{parafovea}}$ and M_{FAZ} are the mean values within parafoveal annulus shown in green and FAZ shown in white (Fig. 9(A1)), respectively, and σ_{FAZ} is the standard deviation of values within FAZ.

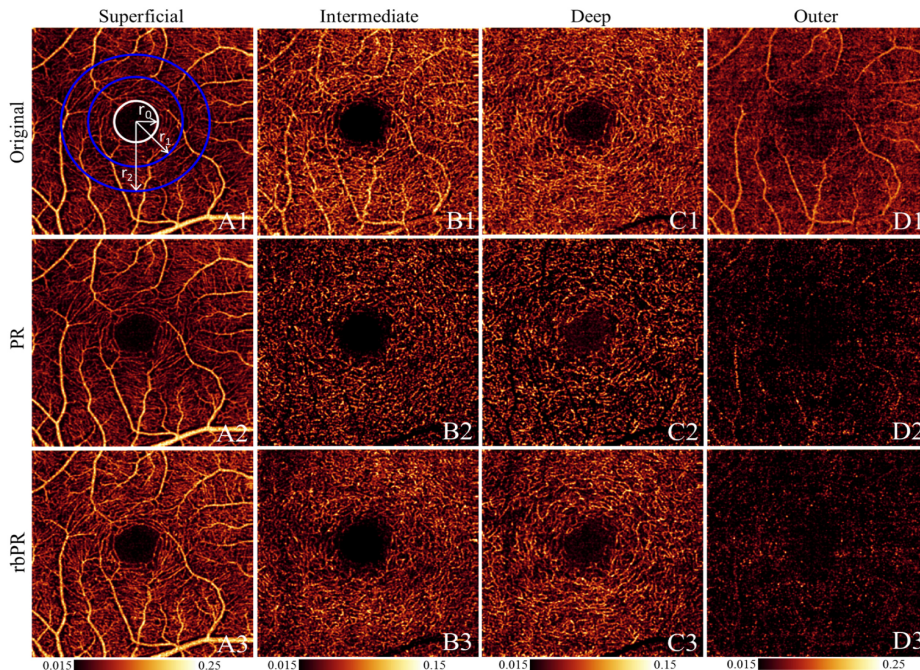


Fig. 9. A comparison of retinal OCTA ($3 \times 3\text{mm}$) from a normal participant processed without projection suppression (original, row 1), with projection suppressed by the prior projection-resolved method (PR, row 2) and the novel reflectance-based PR algorithm (rbPR, row 3). Column A: *En face* OCTA of the superficial vascular plexus. Column B: *En face* OCTA of the intermediate capillary plexus. Column C: *En face* OCTA of the deep capillary plexus. Column D: *En face* OCTA of the outer retinal slab. In A1, white circle ($r_0 = 0.3\text{mm}$) and blue ring ($r_1 = 0.65\text{mm}$, $r_2 = 1\text{mm}$) mark the foveal avascular area and parafoveal annulus for the measurement of flow signal to noise ratio below.

To quantitate the remaining artifact level, important in accurate detection and quantification of choroidal neovascularization in the normally avascular outer retinal slab, we calculated the remaining artifacts in outer retina normalized by inner retinal flow signal in parafovea, as

$$RA = \frac{M_{\text{Outer}} + 3 \times \sigma_{\text{Outer}}}{M_{\text{Inner}} + 3 \times \sigma_{\text{Inner}}} \quad (7)$$

where, M_{Outer} and M_{Inner} are the mean values of outer and inner retina within the parafovea, σ_{Outer} and σ_{Inner} are the standard deviation of values of the outer and inner retina within the parafovea.

The rbPR method showed improvement over prior PR-OCTA in vascular skeleton area, vascular connectivity and fSNR on three plexuses angiograms and the decrease in remaining artifacts on outer retinal angiogram from the 15 healthy subjects scanned on central macular area ($3 \times 3\text{ mm}$) (Table 1).

Table 1. Comparison between prior PR and rbPR on quantitative metrics

		PR	rbPR	improvement
Superficial	VSA(mm^2)	1.79 ± 0.21	2.30 ± 0.24	64.55%
	VC	0.96 ± 0.02	0.98 ± 0.01	2.08%
	fSNR	3.82 ± 0.91	5.85 ± 1.60	53.14%
Intermediate	VSA(mm^2)	1.96 ± 0.24	2.54 ± 0.15	29.59%
	VC	0.93 ± 0.03	0.98 ± 0.01	5.37%
	fSNR	3.21 ± 0.92	5.82 ± 1.67	81.3%
Deep	VSA(mm^2)	1.29 ± 0.34	1.93 ± 0.65	49.61%
	VC	0.80 ± 0.08	0.95 ± 0.05	18.75%
	fSNR	1.49 ± 0.80	4.6 ± 1.74	208.72%
Outer	RA	0.50 ± 0.09	0.37 ± 0.05	25.92%

VSA: Vascular skeleton area, VC: Vascular connectivity, fSNR: flow single-to-noise ratio, RA: remaining artifact.

4.2 Preservation of choroidal vascularization in age-related macular degeneration

With OCTA, CNV is detected as the presence of pathologic vessels in the normally avascular outer retinal slab. OCTA derived quantitative metrics are important for assessing the effectiveness of anti-angiogenic therapy and monitoring recurrent growth of CNV [5, 6, 13–15]. The vascular integrity is critical in accurately detecting CNV. PR-OCTA removes strong projection artifacts in the RPE layer while preserving the CNV. However, the vascular continuity of the CNV was not always preserved and the background noise remained (Fig. 10(B1)). The rbPR method (Fig. 10(C1)) suppressed the background noise better and delineated CNV with better vascular integrity. This result may be used with additional image processing steps such as saliency-based algorithm, to further remove the background and detect CNV network.

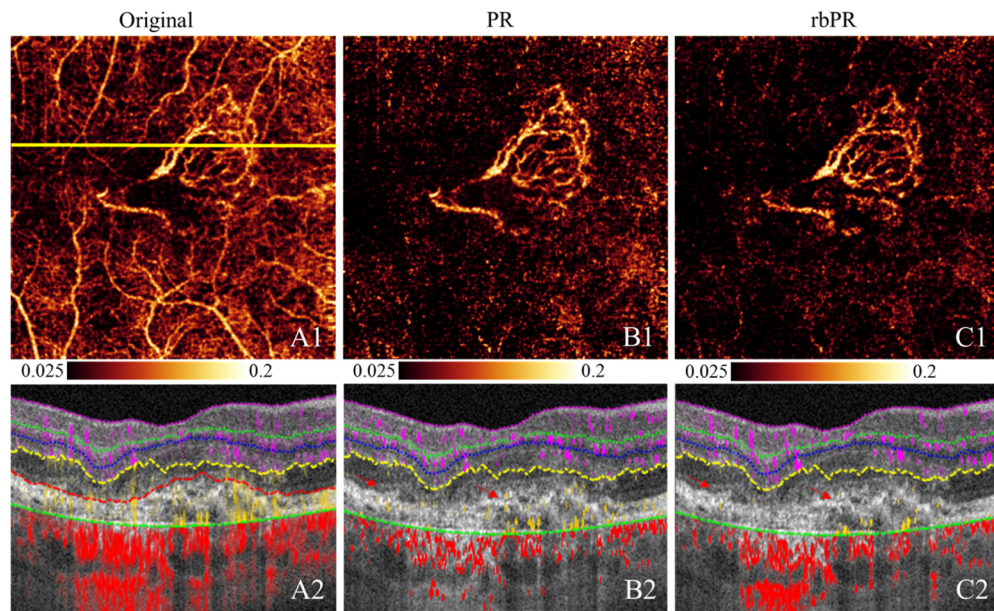


Fig. 10. A comparison of projection-resolved (PR) algorithms in the visualization of choroidal neovascularization (CNV) on both *en face* ($3 \times 3\text{mm}$) and cross-sectional OCTA. (A1) and (A2) are *en face* and cross-sectional OCTA of the outer retinal slab without projection suppression, respectively. (B1) and (B2) are projection suppression with the prior PR algorithm. (C1) and (C2) are projection suppression with the proposed reflectance-based PR (rbPR) algorithm. The projection artifacts persistent on prior PR-OCTA were removed by rbPR (indicated by red arrows).

The cross-sectional angiograms of CNV are critical in classifying the type of CNV anatomically. This is difficult to do without projection removal, as unprocessed OCTA (Fig. 10(A2)) shows artefactual flow both above and below the RPE making classification difficult. The PR method facilitated the interpretation of CNV classification by removing these artifacts. The rbPR demonstrates sub-RPE flow more clearly, classifying the lesion as type 1 CNV. This is consistent with the FA diagnosis.

4.3 Preservation of retinal deeper plexuses in diabetic retinopathy

The ability to observe abnormalities in individual capillary networks may enable earlier detection of diabetic retinopathy. The deeper plexus slabs in conventional OCTA (Fig. 11(B1) and 11(C1)) have significant projection artifacts, making interpretation difficult. PR-OCTA discriminate three distinct retinal plexuses. In diabetic retinopathy, vascular abnormalities have been detected within each individual plexuses with PR-OCTA, findings not possible with conventional OCTA [16, 17].

In a diabetic retinopathy case, applying prior PR-OCTA with lower resolution 6×6 mm scans reduces projection artifact at the expense of reduced vessel connectivity in the deep capillary plexus (Fig. 11(B2) and 11(C2)). In contrast, rbPR (Fig. 11(B3) and 11(C3)) resulted in maintained vessel integrity and improved contrast, features important for detecting and quantifying deep capillary plexus abnormalities.

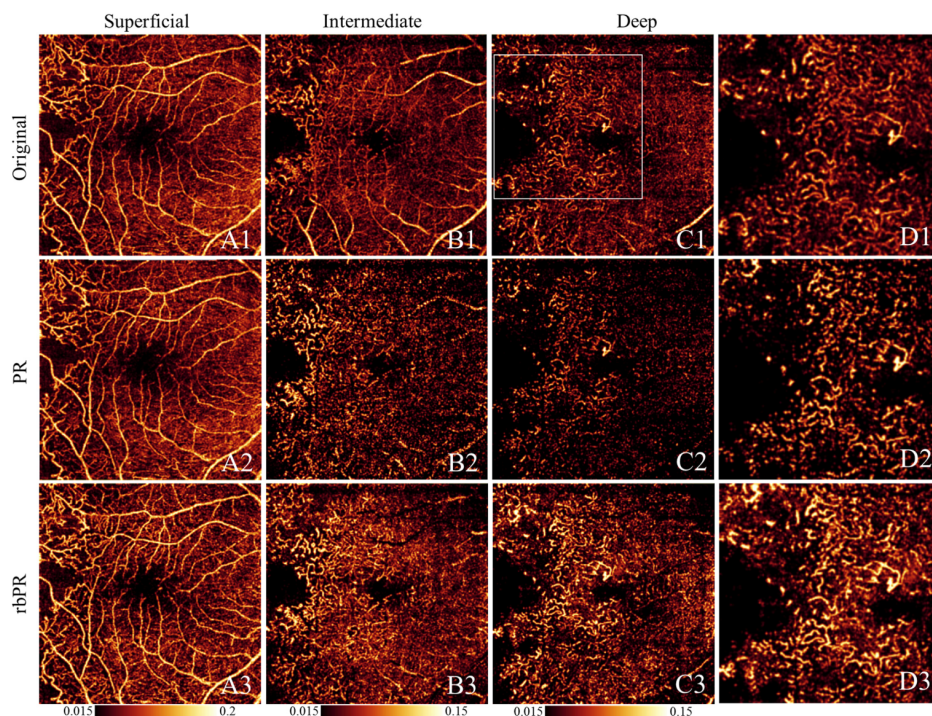


Fig. 11. A comparison of retinal OCTA (6×6 mm) processed without projection suppression (original, row 1), with projection suppressed by the prior projection-resolved method (PR, row 2) and the novel reflectance-based PR algorithm (rbPR, row 3). Column A: *En face* OCTA of the superficial vascular plexus. Column B: *En face* OCTA of the intermediate capillary plexus. Column C: *En face* OCTA of the deep capillary plexus. Column D: The magnified images in the positions indicated by a white box in C1.

4.4 Preservation of choriocapillaris

The choriocapillaris plays an important role in many macular diseases [18, 19]. However, *in vivo* imaging of the choriocapillaris using OCTA is hindered by projection artifacts. The PR method applied to the choriocapillaris slab (BM to 15 μm below) at central macula (Fig. 12(B1)), suppressed these artifacts. The rbPR also suppresses these projection artifacts (Fig. 12(C1)) but shows a denser and more continuous mesh-like vascular network with small black pores where blood flow is absent, which better reflects the known scanning electron microscopy description of the vasculature [20].

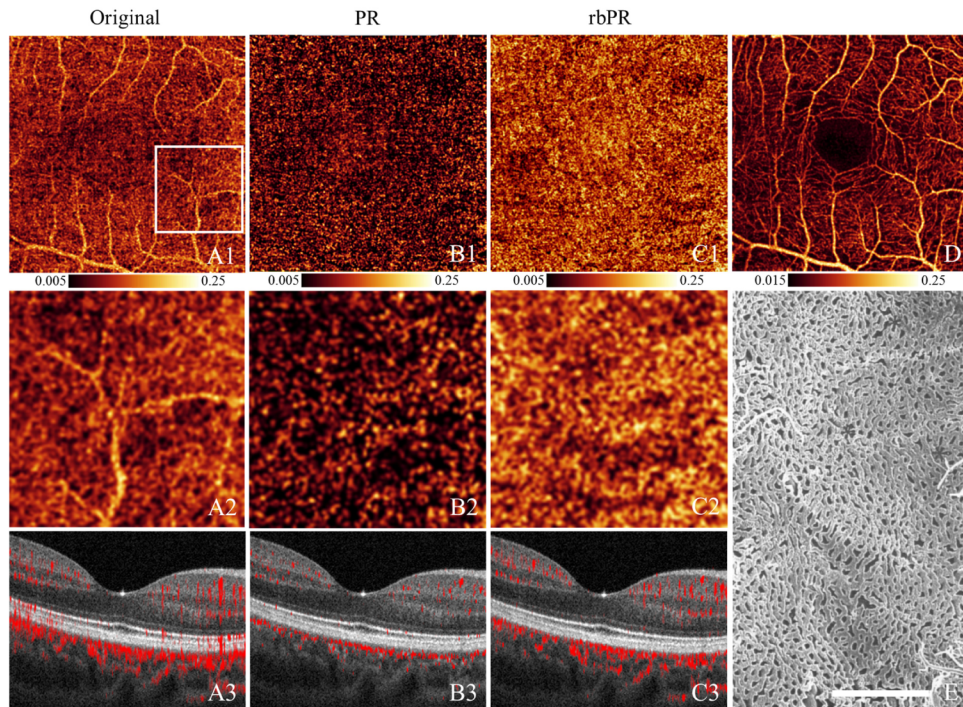


Fig. 12. A comparison of submacular choriocapillaries OCTA processed without projection suppression (column A), with projection suppressed by the prior projection-resolved method (PR, column B) and the novel reflectance-based PR algorithm (rbPR, column C). (A1-C1): *En face* OCTA of the choriocapillaries plexus. (A2-C2): The magnified images in the positions indicated by a white box in A1. (A3-C3): B-scan reflectance image overlaid with flow signal. (D) inner retinal angiogram. (E) choriocapillaris shown by scanning electron microscopy, reproduced from Olver et al. with permission [20]. The scale bar is 250 μm .

5. Discussion and conclusion

In this study, we demonstrated a novel PR algorithm – rbPR which removes flow projection artifact and preserve *in situ* blood flow in OCTA better than prior methods. Several novel ideas were applied on rbPR algorithm. First, we take into account OCT reflectance information in distinguishing the real vessels and flow projection on OCTA. This improved the reliability of projection resolution, compared to the methods that solely depend on OCTA. Second, the non-linear model was applied for generating the vascular contrast enhanced map and vascular probability distribution map based on OCT reflectance. This improved the vascular continuity, compared to the linear fashion method we used before. Third, instead of the processing based on single A-line, we analyzed 2D images in transverse direction slice by slice to separate *in situ* flow and projection artifacts. This helps to preserve the continuity of

vascular networks. Forth, the projection resolution under larger vessels was processed separately to minimize the negative artifact and shadowing problem.

Compared to previously published PR method, rbPR algorithm can suppress more flow projection artifacts, especially in the outer retinal slab, while preserving more blood vasculature and remaining more continuous vascular network in deeper plexuses. This is very critical for the development of following automatic quantification softwares, such as CNV detection [5] and nonperfusion area detection on three plexuses [17]. Similar to prior PR method, this new rbPR method also resolves the projection artifacts on a voxel-by-voxel basis. Unlike slab-subtraction algorithm that is only applicable to *en face* view, rbPR allows interpretation of blood flow with respect to retinal plexuses on cross-sectional images. For example, using PR methods, we may be able to distinguish interconnecting vessels between the vascular plexuses.

There remain some limitations to the rbPR method. First, in order to determine the vessel category more accurately, OCT 3D volume was split into two sub-volumes along IS/OS boundary. Although the prior requirement of segmentation on IS/OS is a limitation to this method, IS/OS segmentation is not required completely accurate, which allows the proposed rbPR algorithm could works well on some pathological cases that IS/OS might be missing. Second, a more sophisticated method based on experimental calibration may further improve the artifact removal under large vessels.

Acknowledgments

This work was supported by grant DP3 DK104397, R01 EY024544, R01 EY023285, P30 EY010572 from the National Institutes of Health (Bethesda, MD), and by unrestricted departmental funding from Research to Prevent Blindness (New York, NY). Oregon Health & Science University (OHSU), David Huang and Yali Jia, have a significant financial interest in Optovue, Inc. These potential conflicts of interest have been reviewed and managed by OHSU.